Noise Correction and Length Scale Estimation for Scalar Dissipation Rate Measurements in Turbulent Partially Premixed Flames

Jian Cai · Robert S. Barlow · Adonis N. Karpetis · Chenning Tong

Abstract A recently developed conditional sampling-based method for correcting noise effects in scalar dissipation rate measurements and for estimating the extent of resolution of the dissipation rate is employed to analyze the data obtained in turbulent partially premixed (Sandia) flames. The method uses conditional sampling to select instantaneous fully resolved local scalar fields, which are analyzed to determine the measurement noise and to correct the Favre mean, conditional, and conditionally filtered dissipation rates. The potentially under-resolved local scalar fields, also selected using conditional sampling, are corrected for noise and are analyzed to examine the extent of resolution. The error function is used as a model for the potentially under-resolved local scalar to evaluate the scalar dissipation length scales and the percentage of the dissipation resolved. The results show that the Favre mean dissipation rate, the mean dissipation rate conditional on the mixture fraction, and dissipation rate filtered conditionally on the mixture fraction generally are well resolved in the flames. Analyses of the dissipation rates filtered conditionally on the mixture fraction and temperature show that the length scale increases with temperature, due to lower dissipation rate and higher diffusivity. The dissipation rate is well resolved for temperatures above 1,300 K but is less resolved at lower temperatures, although the probability of very low temperature events is

J. Cai · C. Tong (✉)
Department of Mechanical Engineering,
Clemson University, Clemson, SC 29634-0921, USA
e-mail: ctong@ces.clemson.edu

R. S. Barlow
Combustion Research Facilities, Sandia National Laboratories,
Livermore, CA 94551-0969, USA

A. N. Karpetis
Department of Aerospace Engineering, Texas A&M University,
College Station, TX 77843, USA

low. To fully resolve these rare events the sample spacing needs to be reduced by approximately one half. The present study further demonstrates the effectiveness of the new noise correction and length scale estimation method.

1 Introduction

The scalar dissipation rate is a key variable characterizing turbulent mixing. It is also an important variable in studying and modeling turbulent nonpremixed/partially premixed flames [1, 2]. The mean scalar dissipation rate, $\langle \chi \rangle = \langle 2D\nabla\xi \cdot \nabla\xi \rangle$, appears in the scalar variance equation as the rate of reduction of the variance of scalar fluctuations by mixing, where D, χ, and ξ are the molecular diffusivity, the scalar dissipation rate, and the scalar variable, respectively. The mean scalar dissipation rate conditional on the scalar value, $\langle \chi | \xi \rangle$, is the mixing term in the transport equation of the scalar probability density function (PDF) [3]. It is also a key quantity in the conditional moment closure and the laminar flamelet models [2, 4, 5]. Eswaran and Pope [6] were the first to obtain the conditional dissipation rate in a turbulent flow (using direct numerical simulation).

In a turbulent flow or a turbulent flame the scalar (mixture fraction) dissipation rate comes primarily from fluctuations at the smallest length scales. These fluctuations are much smaller than the integral-scale fluctuations. As a result, accurate measurements of the dissipation rate require both high spatial resolution and high signal-to-noise ratio, which are difficult to achieve even at moderate Reynolds numbers. It is, therefore, generally necessary to quantify the effects of measurement resolution and noise on dissipation rate measurements. In a measurement system these effects, however, are usually present at the same time. For example, both the amount of dissipation resolved by the measurement system and the noise contribution increase with the resolution, making their effects difficult to separate and to quantify.

Because of its importance and the difficulties in its measurements, much effort has been devoted to quantifying and improving the accuracy of scalar dissipation rate measurements (e.g., [7–12]). One approach [13, 14] uses Pope's spectral model [15] and a noise model to fit the measurement data, allowing inference of the noise variance and the length scale of the mean scalar dissipation. Several recent studies used redundant signals to separate the noise contributions in thermal dissipation in flames [16–18].

A limitation of spectral approaches is that it cannot be applied to the conditional scalar dissipation rate. In addition, the so-called ramp-cliff scalar structure, which generally consists of two broad region (of the order of an integral length scale) with gradual variations of scalar value (ramps) separated by a thin layer (cliff) with a large jump in the scalar value, is usually present in turbulent passive scalar fields as well as in nonpremixed and partially premixed turbulent flames [19–22]. The cliff is a highly local structure with large dissipation rate, but does not necessarily contribute significantly to the spectrum. Furthermore, the spectrum calculated depends on ratio of the length of the signal record used to compute the spectrum to the thickness of

the cliff. Spectral analysis, therefore, is generally not suited to characterize the length scale of such a highly local structure.

To overcome these difficulties, Cai and Tong [12] developed an analysis approach based on conditional sampling, without using a spectral model or redundant signals. The conditional sampling procedure makes use of the unique properties of turbulent scalar fields to select fully resolved conditional local scalar fields (see Section 2 for details), enabling separation of the noise effects from resolution effects. Noise correction is applied to the fully resolved fields and potentially under-resolved local scalar fields, which also are selected by using conditional sampling. The noise-corrected dissipation rate along with a physical space model is then used to evaluate the extent of resolution of the scalar dissipation rate and the scalar dissipation length scales for these fields. Cai and Tong [12] applied the method to turbulent jets with passive temperature fluctuations and demonstrated its effectiveness.

In present study, we employ the method to analyze the measured scalar dissipation rate in turbulent partially premixed (Sandia) flames [23–25] to correct for noise effects and to evaluate the length scales associated with several types of conditional dissipation rate. The study extends the method to turbulent flames, and provides accurate measurements of important physical variables characterizing the dissipative scales of the flames. The rest of the paper is organized as follows. Section 2 provides a brief description of the method, followed by a summary of the measurement system and experimental data in Section 3. In Section 4 we analyze the fully resolved and potentially under-resolved conditional local scalar fields to extract the noise variance, to perform noise correction, and to estimate the dissipation length scale of the potentially under-resolved fields and the extent they are resolved. We also quantify the extent of resolution of the mean scalar dissipation rate and the conditional dissipation rate. The conclusions are given in Section 5.

2 Brief Description of the Method

In this section we summarize the noise correction and length-scale estimation method developed by Cai and Tong [12]. For more details refer to that reference. The method uses two conditioning variables, the filtered (locally averaged) scalar and the subfilter-scale (SFS) scalar variance (local scalar variance). In turbulent flames the Favre filtered (locally averaged) scalar,

$$\langle \xi \rangle_L \equiv \langle \rho \xi \rangle_\ell / \langle \rho \rangle_\ell, \tag{1}$$

and the Favre SFS scalar variance,

$$\langle \xi''^2 \rangle_L \equiv \langle \rho \xi^2 \rangle_\ell / \langle \rho \rangle_\ell - \langle \xi \rangle_L^2 \tag{2}$$

are used as conditioning variables. Here $\langle \cdot \rangle_\ell$ and $\langle \cdot \rangle_L$ represent a conventional local average, $\int (\cdot) G(\mathbf{x} - \mathbf{x}') d\mathbf{x}'$, and a Favre local average respectively, and G is the top-hat filter function. A local conditional field spanning the filter domain is selected if the instantaneous values of the values of the conditioning variables satisfy certain criteria.

The most unique aspect of the present method is that rather than analyzing turbulent scalar fields as a general random process (e.g, using only the spectral characteristics), the conditional-sampling procedure makes use of unique aspects of the dynamics of these fields. Previous studies [20–22, 26] have shown that when the SFS variance is small compared to the ensemble mean SFS variance, the local scalar field is well mixed. The statistics of such a conditional scalar is well described by the Kolmogorov–Obukhov–Corrsin theory. The locally averaged scalar dissipation rate and the scalar variance spectral transfer rate are lower than the mean scalar dissipation rate [27]. In the spirit of the Kolmogorov's refined similarity hypotheses, the local conditional Péclet number is expected to be lower than that based on the unconditioned statistics. The scalar dissipation length scales for these fields, therefore, are larger than the mean scalar dissipation length scale [12]. By choosing sufficiently small SFS variance values, one can select local scalar fields with sufficiently large dissipation length scales so that they are well resolved by the measurement apparatus.

For SFS variance much larger than the mean SFS variance, the local scalar is highly segregated and contains the ramp-cliff structure [19–22]. The cliff results from the advective (strain rate)–diffusive balance and has a large jump in the scalar value. Thus, it generally has a large dissipation rate and a small length scale [19–22]. Using different SFS variance values, we can select local scalar fields that can be well resolved and those that are potentially under-resolved to evaluate their dissipation length scales. The well-resolved local fields are used to evaluate the measurement noise variance, which is then used to remove the noise contributions from the potentially under-resolved scalar fields, effectively separating the noise effects from the resolution effects.

For many measurement systems, including the one used to obtain the one-dimensional images in the Sandia flames [23, 24], the noises at different measurement locations (pixels) are uncorrelated random variables and are additive to the scalar values:

$$\xi = \xi^* + n. \tag{3}$$

where ξ^*, ξ, and n are the true scalar value, the measured value, and the noise, respectively. To make noise corrections the noise variance is needed. For the Sandia system, the noise in the measured mixture fraction is dominated by shot noise in the measurement of the major species. The mixture fraction is calculated using Bilger's formula [28] from the C and H elemental mass fractions, both originated from the fuel stream (oxygen is excluded, see [24]). As a result, we expect the noise variance to increase with the mixture fraction (in the cold fuel-air mixture it is proportional to mixture fraction), and therefore, model it as proportional to mixture fraction. We make this first-order approximation because determining experimentally the dependencies of the noise variance on the mass fractions of the major species requires a much larger data set due to the necessity to compute conditional statistics of high dimensions. In this model the dependence of the noise variance on temperature is taken into account by considering the dependencies of the Raman scattering signal levels on the mixture density. Because the species number densities are proportional to the mixture density, so is the total scattering signal and is

the noise variance. Consequently, the model noise variance for the normalized signal (ξ) is inversely proportional to the density, hence is proportional to the temperature, because pressure variations are small in low-speed flows. The variance of the noise is then modeled as proportional to both the mixture fraction and the temperature,

$$\langle n^2 | \xi, T \rangle = \sigma_n^2(\xi, T) = B \cdot \xi \cdot T, \tag{4}$$

where B is a coefficient depending on the characteristics of the measurement system. The value of B is determined in Section 4.1, which agrees well with unpublished data obtained using the same measurement system in steady laminar flames. The model is verified further a posteriori using the corrected dissipation rate (see Sections 4.1 and 4.2).

To obtain the scalar dissipation rate numerical (usually finite difference) schemes are usually needed to calculate the derivatives as experimental data are generally discrete samples. Different schemes involve different numbers of samples and different weights to the samples. Consequently, the calculated scalar dissipation rate and the noise contributions are scheme dependent. A generalized form of an explicit central finite difference scheme for the derivative is

$$h \cdot \frac{\widetilde{d\xi}}{dx} = a_1(\xi_1 - \xi_{-1}) + a_2(\xi_2 - \xi_{-2}) + a_3(\xi_3 - \xi_{-3}) + a_4(\xi_4 - \xi_{-4}) + \dots \tag{5}$$

where h and $\frac{\widetilde{d\xi}}{dx}$ are the distance between adjacent samples (sample spacing) and the estimated derivative, respectively. The schemes used in the present study and their coefficients are given in Table 1.

By including the noise model in the finite difference scheme in (5), the measured derivative is

$$h \cdot \frac{\widetilde{d\xi}}{dx} = a_1(\xi_1 - \xi_{-1}) + a_2(\xi_2 - \xi_{-2}) + a_3(\xi_3 - \xi_{-3}) + a_4(\xi_4 - \xi_{-4}) + \dots$$

$$= a_1(\xi_1^* - \xi_{-1}^*) + a_2(\xi_2^* - \xi_{-2}^*) + a_3(\xi_3^* - \xi_{-3}^*) + a_4(\xi_4^* - \xi_{-4}^*) + \dots$$

$$+ a_1(n_1 - n_{-1}) + a_2(n_2 - n_{-2}) + a_3(n_3 - n_{-3}) + a_4(n_4 - n_{-4}) + \dots$$

$$= h \cdot \frac{\widetilde{d\xi^*}}{dx} + a_1(n_1 - n_{-1}) + a_2(n_2 - n_{-2}) + a_3(n_3 - n_{-3}) + a_4(n_4 - n_{-4}) + \dots, \tag{6}$$

Table 1 Coefficients for central finite difference schemes

Order	a_1	a_2	a_3	a_4	a_5
2	1/2	0	0	0	0
4	8/12	−1/12	0	0	0
6	45/60	−9/60	1/60	0	0
8	672/840	−168/840	32/840	−3/840	0
10	2,100/2,520	−600/2,520	150/2,520	−25/2,520	2/2,520

where $\widetilde{\frac{d\xi^*}{dx}}$ is the estimated derivative without noise. The measured Favre mean dissipation rate is

$$\langle\chi\rangle_F = \langle\rho\chi\rangle/\langle\rho\rangle = \left\langle 2\rho D\left(\widetilde{\frac{d\xi}{dx}}\right)^2\right\rangle/\langle\rho\rangle$$

$$= \left\langle 2\rho D\left(\widetilde{\frac{d\xi^*}{dx}}\right)^2\right\rangle/\langle\rho\rangle + \left\langle\frac{2}{h^2}\sum_{i=-N}^{N}\rho D a_i^2 n_i^2\right\rangle/\langle\rho\rangle$$

$$= \left\langle 2\rho D\left(\widetilde{\frac{d\xi^*}{dx}}\right)^2\right\rangle/\langle\rho\rangle + \frac{2}{h^2}B\sum_{i=-N}^{N}a_i^2\langle\rho D\xi_i^* T_i^*\rangle/\langle\rho\rangle$$

$$\approx \left\langle 2\rho D\left(\widetilde{\frac{d\xi^*}{dx}}\right)^2\right\rangle/\langle\rho\rangle + \frac{2}{h^2}B\sum_{i=-N}^{N}a_i^2\langle\rho D\xi_i T_i\rangle/\langle\rho\rangle$$

$$\approx \left\langle 2\rho D\left(\widetilde{\frac{d\xi^*}{dx}}\right)^2\right\rangle/\langle\rho\rangle + \frac{2}{h^2}BC_N, \tag{7}$$

where $C_N = \sum_{i=-N}^{N}a_i^2\langle\rho D\xi_i T_i\rangle/\langle\rho\rangle$ and $\left\langle 2\rho D\left(\widetilde{\frac{d\xi^*}{dx}}\right)^2\right\rangle/\langle\rho\rangle$ are a scheme dependent factor and the estimated noise-corrected dissipation rate, respectively.

When all the schemes can resolve the turbulence scalar field, the noise-corrected Favre mean dissipation rate does not depend on the scheme. Equation (7) shows that the Favre mean dissipation rate before noise correction, when plotted against C_N, is a straight line with a slope of $\frac{2}{h^2}B$. The intercept of the straight line is the noise-corrected dissipation rate. This linear relationship can be used to determine the noise variance (B in (4)). If the scalar field is not fully resolved by some of the lower-order schemes, then the higher-order schemes that can fully resolve it form a straight line on the $\langle\chi\rangle_F - C_N$ plot. This relationship also can be applied to the Favre conditional dissipation rate and the Favre conditionally filtered dissipation rate.

Using small SFS scalar variance values we can select fully resolved local scalar fields and determine the noise variance using experimental data according to (7). The noise variance is then used to correct the dissipation rate from the potentially under-resolved local scalar fields (large SFS variance). For these fields, the $\langle\chi\rangle_F - C_N$ relationship is not linear. A model for the local scalar profile is needed to evaluate the extent of under-resolution. These local scalar fields contain the ramp-cliff structure, with the cliff having a large dissipation rate and a small length scale. The ramp-cliff structure, therefore, is the primary cause for any under-resolution [12]. Since the cliff is a result of the advective–diffusive balance in the scalar field, the error function is used as a model for the scalar profile [12] to evaluate the extent of under-resolution.

An error-function scalar profile with a width w is

$$\xi(x) = \frac{1}{2} + \frac{1}{2}\text{erf}\left(\frac{x}{w}\right) = \frac{1}{2} + \frac{1}{\sqrt{\pi}}\int_0^{\frac{x}{w}}e^{-x'^2}dx'. \tag{8}$$

The dissipation rate is calculated at $\xi = 0.5$ where the dissipation is at its maximum. Here w corresponds to the $1/e$ point of the maximum scalar derivative. A comparison

among the dissipation rate calculated using a number of selected schemes is shown in Fig. 10 of [12], which is similar to Fig. 10 of the present paper. For a given scheme, as the distance between adjacent samples, h, increases, the calculated dissipation rate decreases. For a fixed h, higher-order schemes resolve more dissipation rate. By comparing the measured dissipation rate to that calculated from error-function profile using different schemes, the width of the profile, w, can be inferred [12]. The results also provide *a posteriori* justification for the error-function model (see Section 4.3). The percentage of the dissipation resolved can also be estimated using the model.

3 Experimental Data

The experimental data used in this study were obtained in piloted turbulent partially premixed methane flames (Sandia flames D and E, see [23–25] for more details). The fuel stream is premixed CH_4 and air with a ratio of 1:3 by volume. The fuel jet with a diameter $d = 7.2$ mm was mounted approximately 17 cm above the 25 cm^2 exit of a wind tunnel contraction, which supplied a laminar co-flow of air at 0.9 m/s. The jet exit Reynolds numbers for flames D and E are 22,400 and 33,600 respectively.

The measurement system employed combined line-imaging of Raman scattering, Rayleigh scattering, and laser-induced CO fluorescence. Simultaneous measurements of the major species (CO_2, O_2, CO, N_2, CH_4, H_2O, and H_2), the mixture fraction (obtained from all major species), the temperature, and the radial component of scalar dissipation rate were made. As mentioned in Section 2, the mixture fraction is calculated using a variation of Bilger's definition, which has been modified by excluding the oxygen terms [24].

The issue of measurement uncertainty was addressed in [24], which concluded that the accuracy of the measured mixture fraction is sufficient for determining the mixture fraction variance in the flames. For example, the measured values of the scalar (mixture fraction) variance in uniform calibration flows were 10^{-6} in air and 10^{-5} in flat stoichiometric flame products and in jet fluid, respectively, much smaller than the smallest SFS variance values used in this study. Thus, the noise contributions to the mixture fraction and the SFS variance, both conditioning variables, are small (the noise contribution to the scalar dissipation rate is the subject of the present study).

The length of the imaging line is 6.13 mm with a imaging pixel spacing of 0.2044 mm. The SFS scalar variance is calculated using a segment (3.065 mm or 15 pixels) of each line image. Cai and Tong [12] recently showed that the noise variance and the length scales inferred do not depend on the size of the segment. In the analyses 6,000 line images are used at each measurement location. We use a bin width of $\Delta \ln \langle \xi''^2 \rangle = 1.3$. Due to the limited data size, we employ kernel methods to compute the conditional statistics to achieve sufficient statistical convergence.

4 Results

In this section the noise correction and length scale estimation method for mixture fraction dissipation is applied to the Sandia Flames. We first analyze the well-

resolved local scalar fields selected using a small SFS variance value to obtain the noise variance, which is then used to correct for the dissipation rate of these and the potentially under-resolved scalar fields as well as the mean and conditional dissipation rate. The extent of the resolution of these statistics is examined. The potentially under-resolved fields are analyzed using the error-function model. In the present paper all the dissipation rate statistics are Favre statistics; therefore, for convenience we omit the term "Favre" for the rest of the paper.

4.1 Well-resolved local scalar field

The mean dissipation rate conditional on the scalar value obtained from the conditional local scalar fields is the conditionally filtered dissipation rate (see [20]). At each measurement location it is calculated using the five finite central difference schemes (Table 1). Figure 1a shows the results in Flame D at $x/D = 15$ for $\langle \xi \rangle_L =$
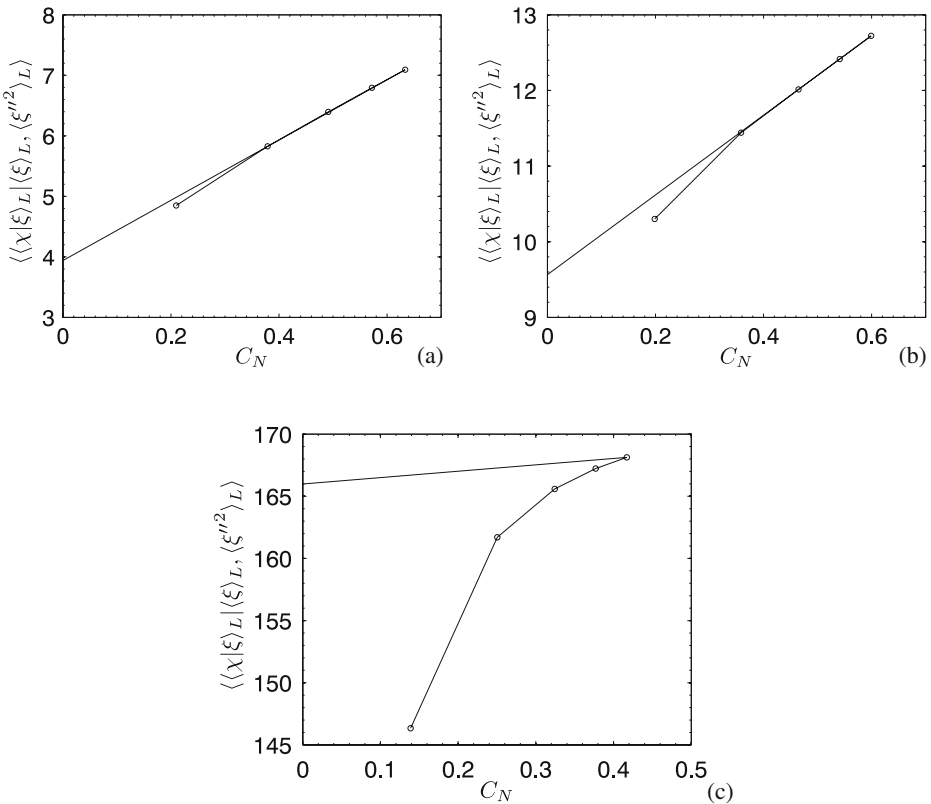
Fig. 1 Conditionally filtered scalar dissipation rate (near the stoichiometric mixture fraction) vs. C_N at $x/d = 15$ in flame D. The data points (increasing C_N) represent the measured dissipation rate using the second- to tenth-order finite differencing schemes, respectively. The intercept of the straight lines represent the noise-corrected dissipation rate. **a** Well-resolved local fields, $\langle \xi''^2 \rangle_L = 5.2 \times 10^{-4}$; **b** under-resolved by the second-order scheme, $\langle \xi''^2 \rangle_L = 2.6 \times 10^{-3}$; **c** potentially under-resolved local fields, $\langle \xi''^2 \rangle_L = 6.7 \times 10^{-2}$

0.35 and $\langle \xi''^2 \rangle_L = 5.2 \times 10^{-4}$, the latter much smaller than the mean SFS variance (2.36×10^{-2}). As the scheme order increases, the conditionally filtered dissipation rates increases. The dissipation-C_N relationship essentially is linear, indicating that the increases in the dissipation rate values using the higher-order schemes come from increased noise contributions (7); therefore, the local scalar fields for small SFS variance are well resolved by all the schemes. Note that the noise-corrected conditionally filtered dissipation (the intercept) is of the same order as the noise contributions.

For a somewhat larger SFS variance, $\langle \xi''^2 \rangle_L = 2.6 \times 10^{-3}$ (Fig. 1b), the data points obtained using the fourth- and higher-order schemes form a straight line while the dissipation rate using the second-order scheme is below this line, indicating that the higher-order schemes are capable of resolving the smallest scalar length scale in these conditional fields but second-order scheme is not. The intercept of the straight line ($\sim 9.58 \text{ s}^{-1}$) is lower than the dissipation rate calculated using the second-order scheme ($\sim 10.22 \text{ s}^{-1}$), indicating that when using second-order scheme the effect of the noise is greater than that of the insufficient resolution. The constant B in the noise variance model is determined as 1.2×10^{-7}. This value is consistent with the noise variance obtained in a laminar flame at Sandia (unpublished data). We also obtained the conditional noise variance on both the mixture fraction and temperature (the left-hand-side of (4)) from the data (not shown). The results agree well with the model except for the $\xi = 0.5$–0.6 range, in which the noise variance is larger than the model prediction for a maximum of approximately 15%. Thus, even in this mixture fraction range the noise correction procedure is able to remove more than 85% of the noise contribution to the scalar dissipation rate. Elsewhere the model is accurate to within the statistical uncertainty in determining the dissipation rate. These results provide an *a posteriori* justification for the noise model.

For large SFS variance, $\langle \xi''^2 \rangle_L = 6.7 \times 10^{-2}$ (Fig. 1c), the dissipation-C_N plot is curved. A straight line going through the data point for the tenth-order scheme and having the same slope (coefficient B) as in Fig. 1a, b is also shown. The data points for the eighth- and lower-order difference schemes would have followed a straight line if the dissipation rate were fully resolved by the schemes. The fact that these points are below the straight line indicates that these schemes are resolving less dissipation rate than the tenth-order scheme. Note that the dissipation rate using the second- and fourth-order schemes is less than the intercept of straight line ($\sim 166.0 \text{ s}^{-1}$), indicating that even the uncorrected results are underestimating the dissipation rate. We cannot, however, determine from this figure whether the tenth-order scheme is capable of fully resolving the scalar scales. This case will be analyzed using the error-function model in Subsection 4.3.

4.2 Noise corrections

The dissipation rate filtered conditionally on the mixture fraction using schemes of different orders for three different SFS scalar variance values, $\langle \xi''^2 \rangle_L = 5.2 \times 10^{-4}$, 2.6×10^{-3} and 6.7×10^{-2}, is given in Figs. 2a, 3a and 8a respectively. We subtract the noise contributions and show the results in Figs. 2b, 3b and 8b. For small SFS scalar variance ($\langle \xi''^2 \rangle_L = 5.2 \times 10^{-4}$, Fig. 2), the corrected dissipation rate values calculated using second-to tenth-order schemes largely overlap, indicating that all the schemes are sufficient to resolve the smallest scalar dissipation length scale in these
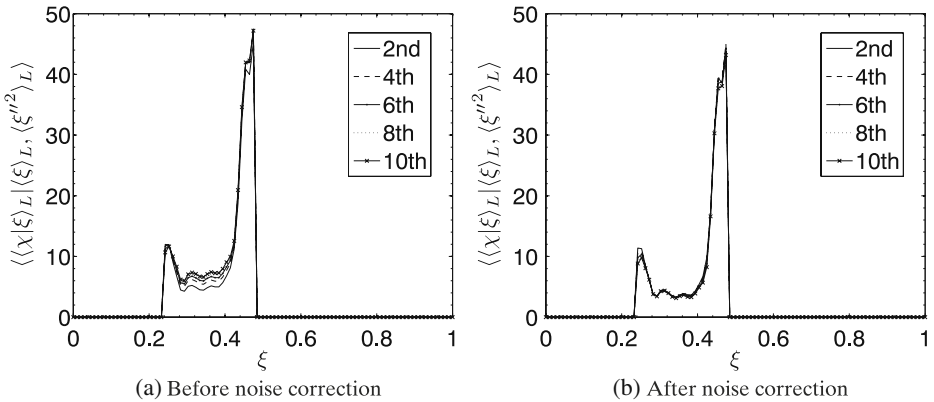
Fig. 2 Conditionally filtered dissipation rate before and after noise correction at $x/d = 15$ in flame D. Small SFS variance ($\langle \xi''^2 \rangle_L = 5.2 \times 10^{-4}$)

local scalar fields and that the noise contributions have been removed. Increasing the SFS scalar variance to $\langle \xi''^2 \rangle_L = 2.6 \times 10^{-3}$ (Fig. 3), the conditionally filtered dissipation rate values using fourth- or higher-order schemes overlap, again indicating sufficient resolution and effective noise correction. These results also demonstrate a posteriori that the noise model in (4) provides an excellent overall approximation of the noise variance. Note that for $0.2 < \xi < 0.45$, the second-order scheme only slightly under-resolves the scalar but for $\xi > 0.45$, the deviations from the other schemes are larger. These deviations are likely a result of the noise variance for these mixture fraction values slightly differing from the model given by (4).

The noise correction procedure also can be applied to the mean scalar dissipation rate, $\langle \chi \rangle_F$, and the conditional dissipation, $\langle \chi | \xi \rangle_F$. The mean dissipation rate profiles at the three downstream locations ($x/d = 7.5$, 15, and 30) in both flames D and E are shown in Fig. 4. The noise-corrected profiles using the tenth-order scheme at
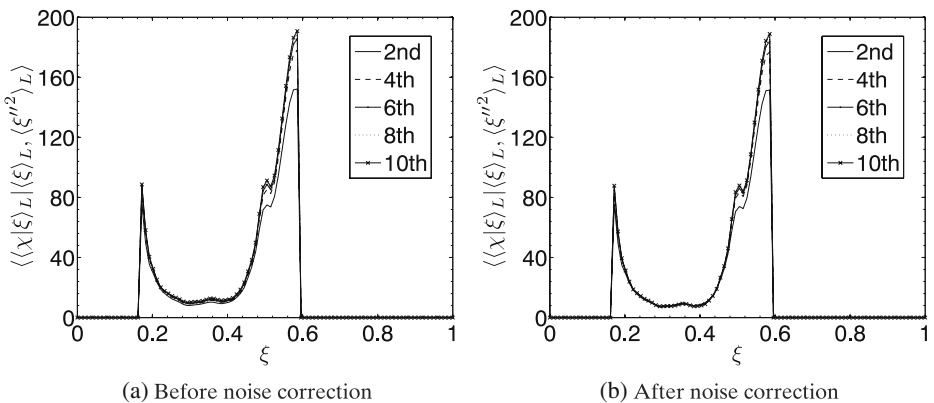
Fig. 3 Conditionally filtered dissipation rate before and after noise correction at $x/d = 15$ in flame D. Medium SFS variance ($\langle \xi''^2 \rangle_L = 2.6 \times 10^{-3}$)
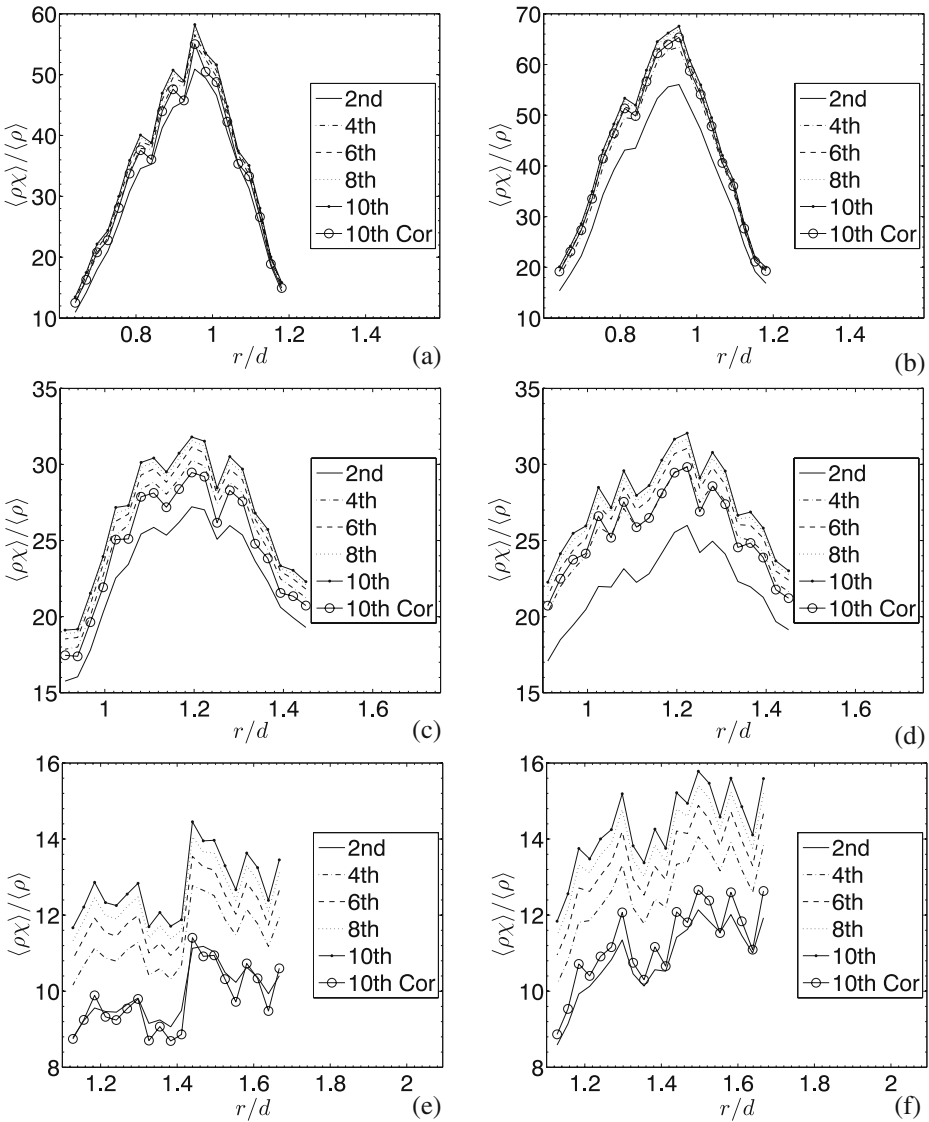
Fig. 4 Measured mean dissipation rate profiles. The *curves with circles* are noise-corrected profiles obtained using the tenth-order scheme. **a**, **c**, **e** Flame D at $x/d = 7.5$, 15, and 30 respectively; **b**, **d**, **f** flame E at the same locations

$x/d = 30$ are close to the uncorrected ones using the second-order scheme, whereas at $x/d = 7.5$ they are close to those using the fourth- or sixth-order schemes, because for the former the resolution is expected to be better due to the larger dissipation length scale. These profiles are in general agreement to those obtained using filtering and extrapolation in Fig. 5 of [29]. The measured peak mean dissipation rate is plotted against C_N in Fig. 5. The dashed lines start from the data points for the tenth-

Fig. 5 Measured mean dissipation rate (1/s) vs. C_N at $x/d = 7.5$, 15, and 30 in flames D and E. The intercept of each dashed straightline is the noise-corrected mean dissipation rate
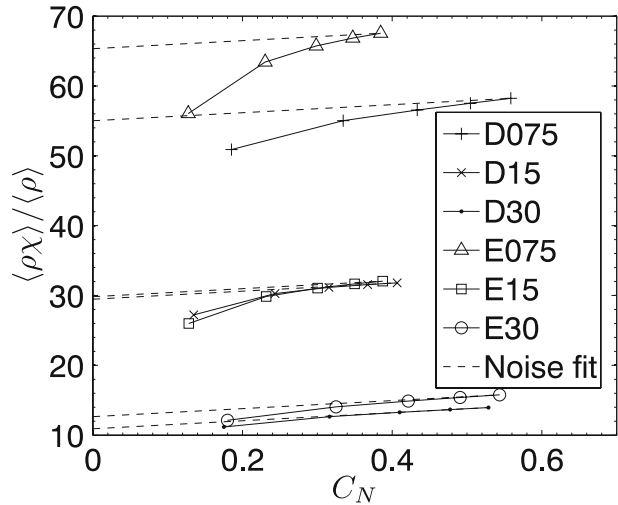
order scheme with the same slope (B in the noise model) as that Fig. 1a, representing the measured dissipation rate by the lower-order schemes if these schemes could fully resolve the dissipation rate, i.e., the measurements were only affected by the noise. Perhaps with the exception of flame E at $x/d = 7.5$, the dissipation rate values obtained by the eighth-order scheme are well within a fraction of 1% of the tenth-order results, indicating that the mean dissipation rate is well resolved by the eighth- and tenth-order schemes.

The results for the measured conditional dissipation rate are shown in Fig. 6. Except at $x/d = 7.5$, the conditional dissipation rate is double-peaked with a minimum slightly to the rich side of the stoichiometric mixture fraction (0.351). At $x/d = 15$ the rich-side peaks are higher than the lean-side ones. The results are in general agreement with those in [30] The lean-side peak conditional dissipation rate vs. C_N are shown in Fig. 7. The ξ values (see the captions) corresponding to the lowest ratio between the dissipation rate values obtained using the second- and tenth-order schemes. Again, perhaps except for flame E at $x/d = 7.5$, the conditional dissipation is well resolved. The difference between the eight-and tenth-order results near the rich-side peak is again likely due to the noise variance slightly deviating from the noise model in that mixture fraction range.

4.3 Estimations of length scales and the extent of resolution for under-resolved scalar field

As shown in the previous subsection, for large SFS variance the local scalar fields are potentially under-resolved. In this subsection we estimate the length scales associated with these fields and the extent to which they are resolved.

For large SFS scalar variance ($\langle \xi''^2 \rangle_L = 6.7 \times 10^{-2}$), although Fig. 8 shows that the conditionally filtered dissipation rate values using different schemes are closer after the noise correction, lower-order schemes still give lower dissipation rates. The conditionally filtered dissipation rate at other locations and in flame E is shown in Fig. 9.
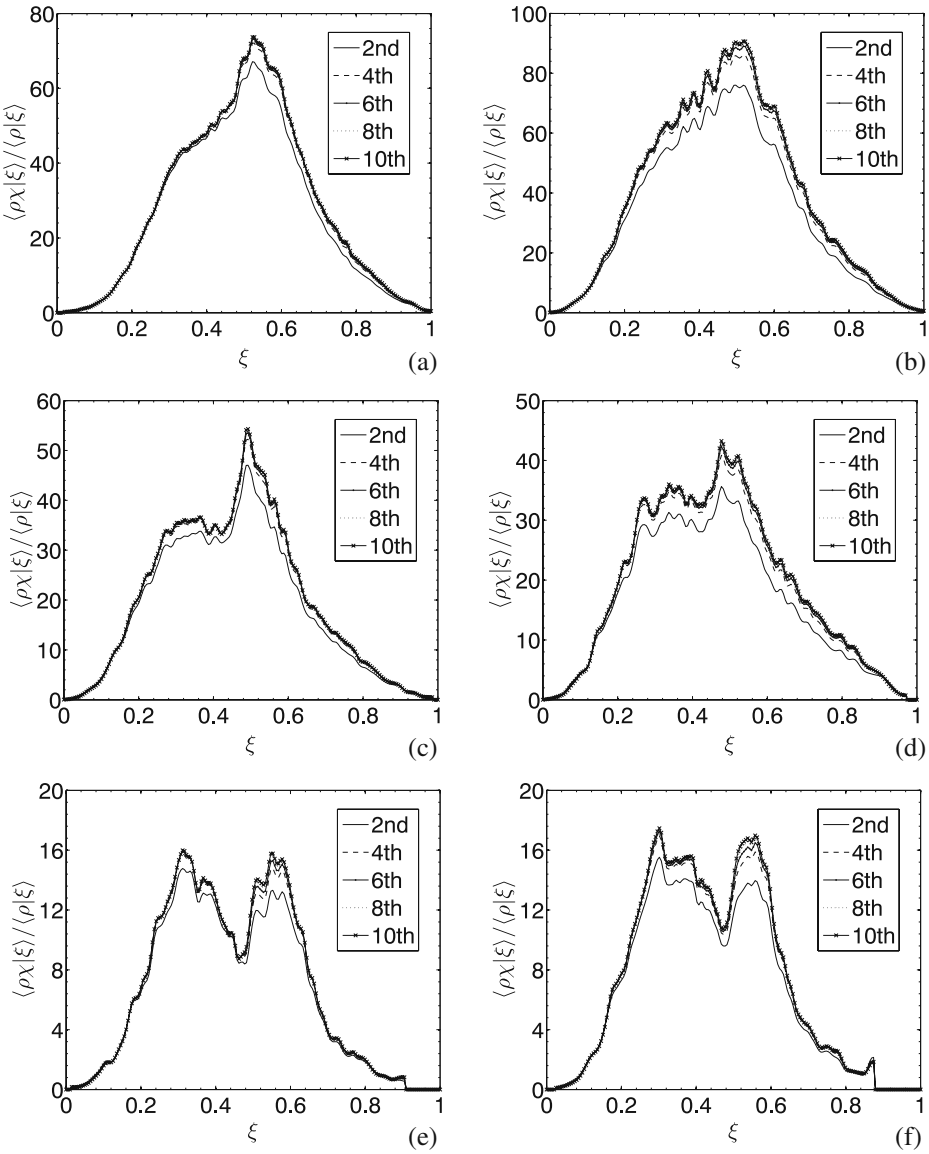
Fig. 6 Measured conditional dissipation rate (1/s) after noise correction: **a**, **c**, **e** flame D at $x/d = 7.5$, 15, and 30 respectively; **b**, **d**, **f** flame E at the same locations

After correcting for the noise, the measured dissipation rate is only affected by the resolution, which is expected to be worst when the SFS scalar variance is largest, due to the sharp cliffs in the local scalar. Because the scalar dissipation length scales are not known *a priori*, they need to be inferred from the experimental data. Comparing the measured scalar spectrum to a model spectrum can provide an estimate of the average dissipation length scale, but not that of the cliffs, which dominate the scalar dissipation rate for large SFS variance. As mentioned in Section 2, to estimate the
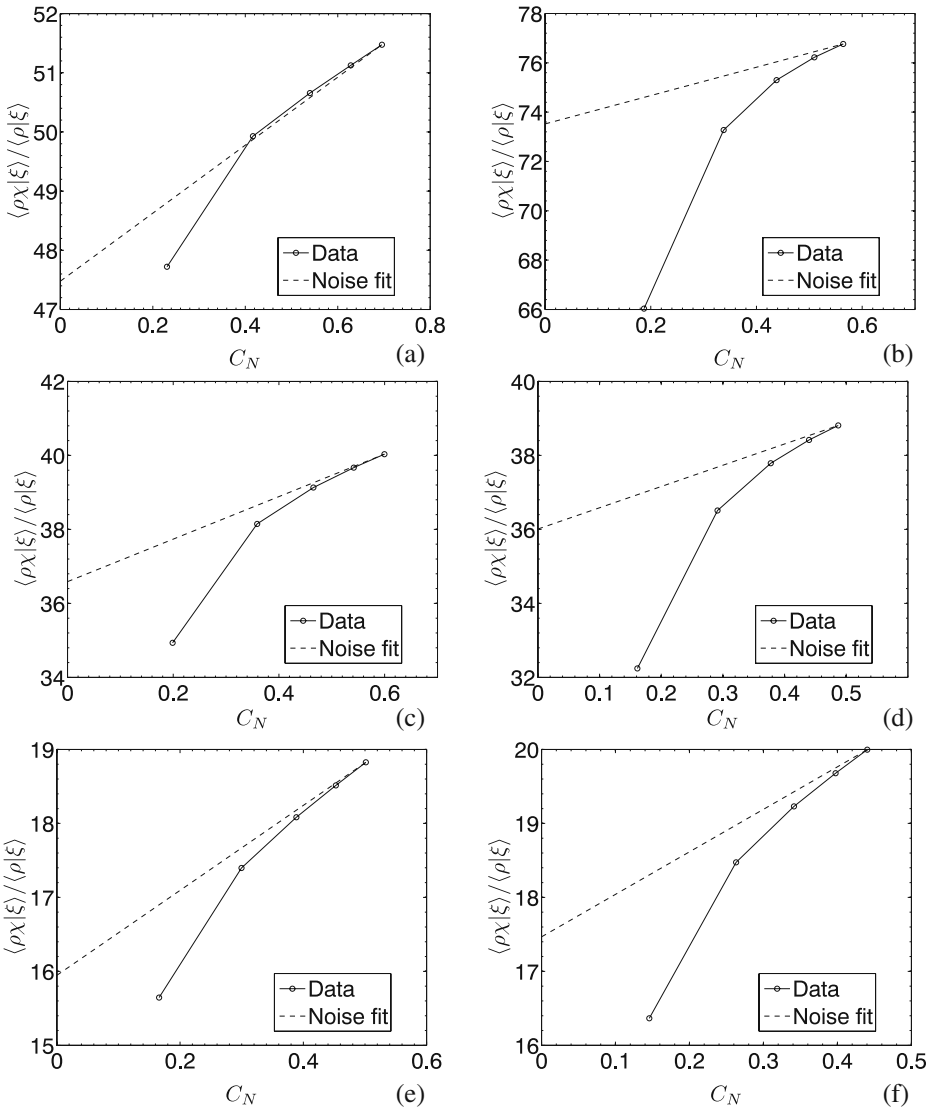
Fig. 7 Measured conditional dissipation rate (1/s) vs. C_N: **a**, **c**, **e** flame D at $x/d = 7.5$, 15, and 30 with the mixture fraction values at 0.397, 0.367, and 0.317, respectively; **b**, **d**, **f** flame E at the same locations with the mixture fraction values at 0.387, 0.336, and 0.302, respectively

length scale of the cliffs we use the error function as a model for the ramp-cliff structure in the SFS scalar fields, and calculate the dissipation rate using different schemes with a range of sample spacings (spatial resolution) [12].

In the discussion on using finite difference schemes to compute derivatives (5), the effects of finite sample spacing, h, is considered, while the effects of the probe
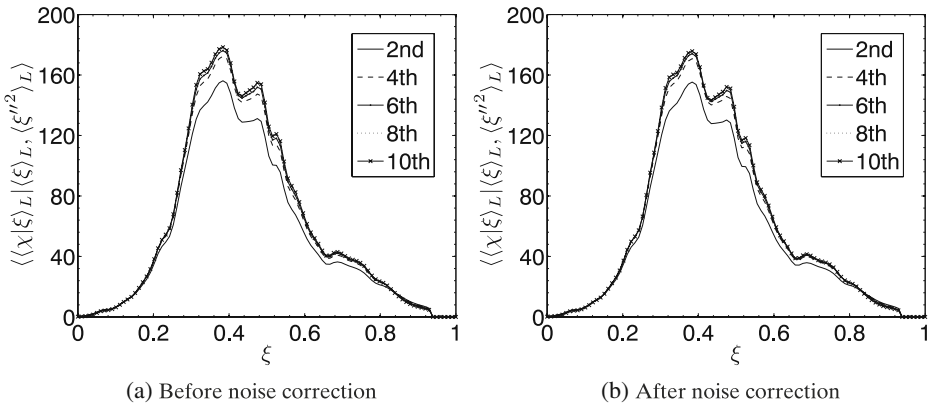
Fig. 8 Conditionally filtered dissipation rate before and after noise correction at $x/d = 15$ in flame D. Large SFS variance ($\langle \xi''^2 \rangle_L = 6.7 \times 10^{-2}$)

volume is not. In Cai and Tong [12], the measurements were made using probes with a size (cold wires of 0.625 μm in diameter) much smaller than the sample spacing (equivalent to 0.307 mm); therefore, the probe sampling volume has negligible effects on the measured dissipation rate. In laser diagnostics, however, the sampling volume (the pixel size) is often comparable to the sample spacing, which also affects the derivative measurements. In the present study the pixel size of the imaging system is approximately the same as the sample spacing (no gap between pixels), and is considered a top-hat filter in physical space. Thus, the samples can be considered to have been taken from the pixel-averaged scalar fields at the center of each pixel. In the following analyses the effects of the pixel filtering on the estimations of the length scales and the dissipation rate are also taken into account.

We use the ratios of the dissipation rate calculated with different schemes to infer the scalar dissipation scale [12]. By equating the ratios from the measured dissipation rate and from the error-function model, a scalar dissipation scale (cliff thickness) can be inferred. To include the effects of pixel averaging, the error function is first pixel-averaged with a pixel size equal to the sample spacing. It then is used to calculate the dissipation rate.

The ratios of the dissipation rate obtained at $x/d = 15$ in flame D are shown in Fig. 10. Here the lowest ratios (at $\xi \approx 0.384$) are compared with the error-function model because these ratios correspond to the smallest scalar length scale. The horizontal axis is the ratio of sample spacing to the scalar profile width, h/w. The ratio of the second- to the tenth-order estimations is approximately 0.883, yielding a h/w values of 0.454 ($w = 0.45$ mm). The scales inferred from all the other schemes also agree very well, indicating the overall success of the noise correction and resolution/length scale estimation, and providing an *a posteriori* justification for using the error function as a model for the ramp-cliff scalar profile.

The inferred length scale and the error-function model can be used to estimate the extent of under-resolution of the ramp-cliff structure. Figure 11 gives the ratio of the dissipation rate of the error-function profile obtained using pixel averaging and finite differencing to the analytically obtained (true) dissipation rate as a function of h/w. At the sample interval of $h/w = 0.454$, the second- through the tenth-order
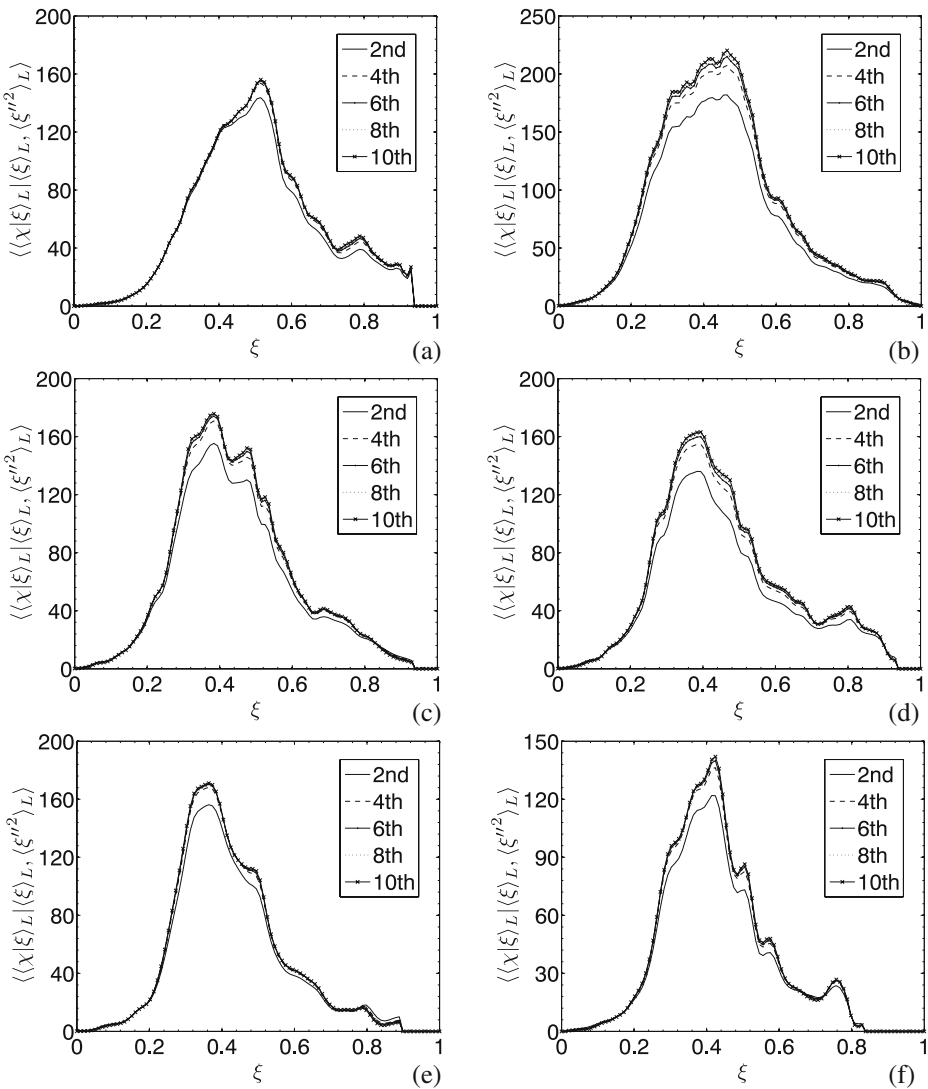
Fig. 9 Conditionally filtered dissipation rate after noise correction. **a**, **c**, **e** Flame D at $x/d = 7.5$, 15, and 30 respectively. The SFS variance values are 6.6×10^{-2}, 6.7×10^{-2}, and 6.3×10^{-2}, respectively; **b**, **d**, **f** flame E at the same locations. The SFS variance values are 8.4×10^{-2}, 5.0×10^{-2}, and 4.5×10^{-2}, respectively

schemes underestimate the dissipation rate by 15.1%, 5.8%, 4.2%, 3.7%, and 3.5%, respectively.

It is interesting to compare these amounts of underestimation to those without considering pixel averaging. Using a figure similar to Fig. 10 (see Fig. 8 in [12]), the same second- to tenth-order ratio of 0.883 gives an h/w value of 0.445, very close to the value of 0.454 obtained above. Thus, for the resolution in the present study (and

Fig. 10 Estimation of the
length scale by comparing the
ratio of dissipation rate
obtained from data (*solid
squares*) to that from the
model (*curves*). The ratios
obtained using different
schemes are shown
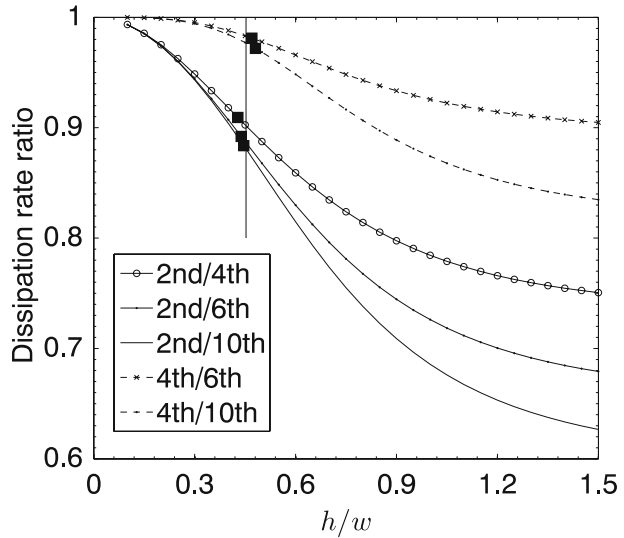
similar resolutions) the estimated length scales are not affected significantly by pixel averaging. A figure similar to Fig. 11 (Fig. 9 in [12]) shows that with this h/w value the schemes underestimate the dissipation rate by 12.1%, 2.5%, 0.8%, 0.3%, and 0.2%, respectively. Consequently, when the finite difference schemes can resolve well the scalar derivative, other effects, such as pixel averaging, can have some influence on the resolution of the scalar dissipation rate.

The 3.3% difference in the resolved dissipation rate for the tenth-order scheme with and without pixel averaging is for local scalar fields with large SFS variance. For the well-resolved local scalar fields, the scalar dissipation length scale is much larger than the pixel size; therefore, the pixel averaging has a negligible effect on the corrected dissipation rate. Consequently, the analysis in Section 4.1 is not affected by the finite pixel size.

The noise-corrected conditionally filtered dissipation rate vs. C_N obtained in both flames D and E are shown in Fig. 12. The mixture fraction values correspond to the peak dissipation rate in Fig. 9. Similar to flame D at $x/d = 15$, in all the other cases the eighth-order scheme resolve slightly less than the tenth-order scheme. Analyses using the error-function model gives a h/w value of 0.40 ($w = 0.511$ mm) at $x/d = 7.5$ and 30 in flame D respectively, corresponding to 97.3% resolution of the dissipation rate. The h/w values for flame E at $x/d = 7.5$, 15, and 30 are 0.594, 0.576, and 0.530 ($w = 0.344$, 0.355, and 0.386 mm) respectively, corresponding to 93.4%, 93.8%, and 95.0% resolution of dissipation rate. These results also indicate that the conditional dissipation rate in Fig. 7 is well resolved because it contains the contributions from both the well-resolved and the potentially under-resolved local fields. The length scales obtained in flame D are approximately 30% larger than those in flame E for all the downstream locations considered. It is interesting to note that the Batchelor scales given in [14] also show an approximately constant ratio for the two flames, although those for flame D are approximately 20% larger than those for flame E.

Fig. 11 Estimation of the resolved dissipation rate obtained using the estimated length scale and the error-function model
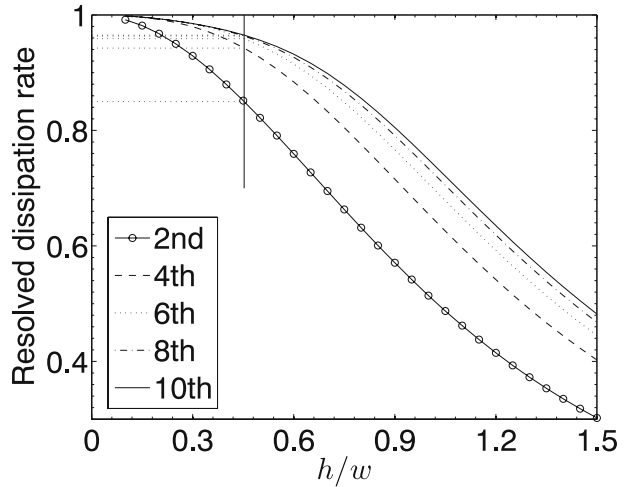
4.4 Dissipation rate filtered conditionally on both mixture fraction and temperature

In the transport equation of the filtered joint density function of mixture fraction and temperature, one of the mixing terms is the scalar dissipation rate filtered conditionally on both mixture fraction and temperature. In this part we examine the dissipation length scale associated with this quantity and the extent to which they are resolved. We focus on the cases with large SFS variance when the smallest length scale and potential under-resolution occur.

When the SFS variance is large, the local SFS scalar fields can contain burning and extinguished flamelets. When the scalar dissipation rate increases, the temperature decreases; therefore, the scalar dissipation length scale is likely to decrease with temperature. The decrease can occur for two reasons: an increased strain rate that results in a higher dissipation rate, and a reduced scalar diffusivity at a lower temperature. As a result, when both the mixture fraction and temperature are used as conditioning variables, estimations of the resolution and length scale need to be performed for a range of temperatures. Here we evaluate the resolution for each error-function profile at the mixture value where the dissipation rate is least resolved. The length scale obtained, therefore, represents the smallest length scale for the dissipation rate.

We compute the ratio of the measured scalar dissipation rate obtained using the second-order scheme to that using the tenth-order scheme at each temperature for the entire range of mixture fraction (Fig. 13). The lowest point at each temperature represents the location (in the scalar space) of the least resolved portion of the scalar profile. This ratio is used with the error-function model to obtain an h/w value and to determine the fraction of the dissipation resolved. The results for Sandia flames D and E at the three downstream locations are shown in Fig 14. In general, h/w decreases (w increases) when the temperature increases, consistent with the properties of laminar flamelets. In some cases we limit the temperature to approximately 1,800 K, because very close to the equilibrium temperatures, the scalar field is well-resolved by both schemes. Thus the ratio is close to unity and is not
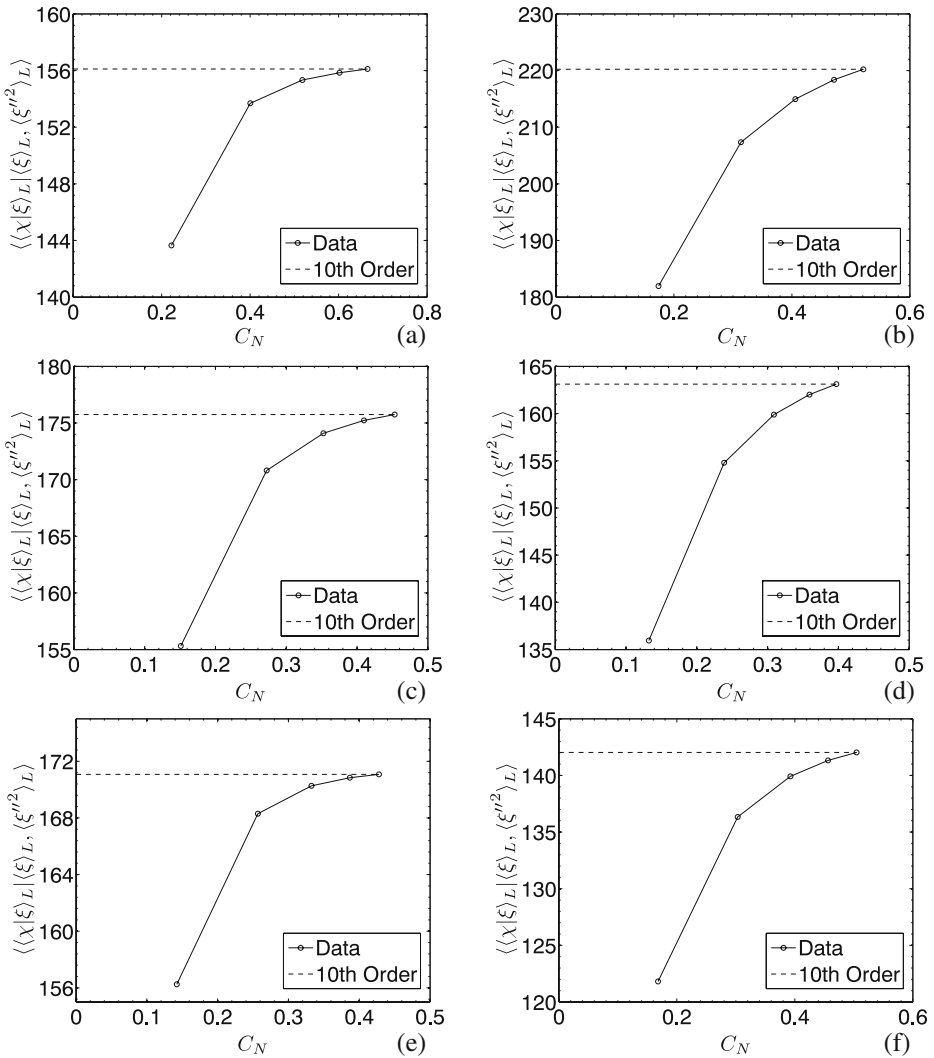
Fig. 12 Conditionally filtered dissipation rate vs. C_N. **a**, **c**, **e** Flame D at $x/d = 7.5$, 15, and 30, respectively. The mixture fraction values are 0.515, 0.384, 0.364 respectively; **b**, **d**, **f** flame E at the same locations. The mixture fraction values are 0.465, 0.394, 0.424 respectively

sensitive to the h/w value (Fig. 11). As a result, at these temperatures the statistical uncertainties in calculating the ratio can have a large impact on the inferred h/w values (e.g., the ratio can exceed unity slightly, for which h/w is not defined). In these cases, however, the scalar is well-resolved and the h/w value is not needed to estimate the dissipation rate.

For flame D at $x/d = 7.5$ the h/w value is approximately 0.30 at 1,850 K (Fig. 14), i.e., the width of the error-function profile is three times the sample spacing. The dissipation rate is more than 98% resolved by the tenth-order scheme (Fig. 15). The h/w value increases to approximately 0.68 at 1,300 K, corresponding to approxi-

Fig. 13 Ratio of the measured dissipation rate using the second-order scheme to that using the tenth-order scheme in flame D at $x/d = 15$. The lowest value at each temperature (near the *dashed line*) represents the least resolved part of the mixture fraction profile
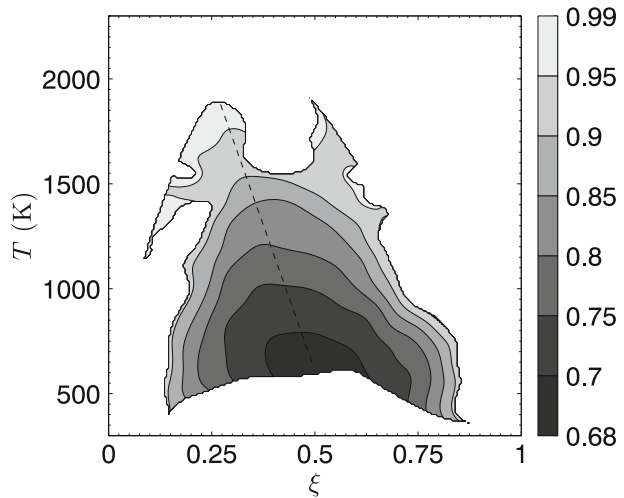
mately 91% resolution of the dissipation rate, and indicating that the measurement resolution is adequate, even for the highest dissipation rate at this location. Moving to $x/d = 15$, h/w is also approximately 0.3 at 1,800 K, again indicating sufficient resolution. The temperature at this location, however, can drop much lower due to the local extinction events. At 700 K, h/w increases to nearly 1.0, corresponding to a much narrower error-function profile due to both high strain rate and reduced diffusivity at low temperatures. Only 72% of the largest dissipation rate is resolved. At this location, the measurement resolution is capable of adequately resolving the dissipation rate down to 1,300 K. Further downstream at $x/d = 30$, where the dissipation rate has reduced, the maximum h/w, which occurs at 1,000 K, is less than 0.75, smaller than those at the upstream locations. Approximately 90% of the dissipation at this temperature is resolved.

The h/w values for flame E are generally higher than those for flame D at the same downstream locations, reflecting the higher Reynolds number for the former. At $x/d = 7.5$ there is already a significant amount of local extinction. The h/w value reaches 1.4 at 770 K, the highest of all cases. Only 52% of the dissipation at this temperature is resolved, the least resolved case. Nonetheless, at 1,800 K, 98% of the dissipation is resolved because the flamelets are expected to be only mildly strained. At $x/d = 15$ and 30, the results are qualitatively similar to those for flame D, with the resolved dissipation rate a few percentages lower.

Overall the smallest length scale in flame E is smaller than that in flame D, consistent with the expected Reynolds number dependence. The results show that to fully resolve the smallest length scale associated with the conditionally filtered dissipation rate in these flames, the pixel size needs to be reduced by approximately one half.

4.5 Discussions

In this paper we have discussed two types of scalar dissipation length scales: one associated with the dissipation rate filtered conditionally on the mixture fraction,

Fig. 14 Length scale of the scalar (ramp-cliff) structure as a function of temperature. The SFS variance values are given in Fig. 8
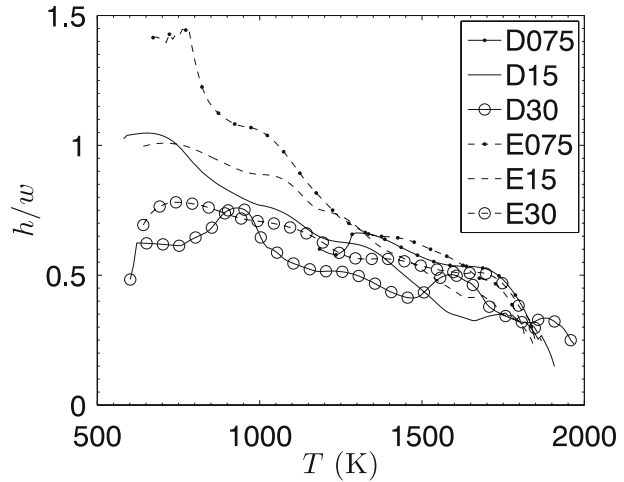
the other filtered conditionally on both the mixture fraction and temperature. The former represents the average dissipation length scale for all the ramp-cliffs in the conditional SFS fields with large SFS variance. The latter further separates the ramp-cliffs according to their peak temperatures, providing more detailed length scale information. These length scales are complementary to the dissipation length scales given in [14], which represents the length scales associated with the mean dissipation rate. In general, for a given random field the length scales for different statistics can be different, and may require different spatial resolution to resolve them fully. It would also be interesting to quantify the distribution of the instantaneous length scales of the scalar fields in a way similar to those of temperature fields [18].

The effects of the finite pixel size were considered along with the finite sample spacing to address the issue of measurement resolution. The effects were accounted for as a pre-sampling (top-hat) filter due to pixels of a finite size; therefore, such a treatment is not limited to pixel filtering nor top-hat filters. It can be generalized, without much difficulty, to include other factors that can be considered pre-sample filtering, such as optical blurring, etc. In the error-function model, a pre-sampling filter can be applied to the error-function profile before the other processing procedures, and therefore, is simple to implement. It is also straightforward to use different filters.

In Cai and Tong [12] a revised error-function model was developed to take into account the fluctuations of the ramp-cliff structure in the mixture fraction space and the dissipation rate due to the background scalar fluctuations. In that study the measurements were made at 80 jet diameters downstream of the nozzle, where the background scalar fluctuations were significant compared to those of the ramp-cliff structure. The data for the present study were obtained within 30 jet diameters from the nozzle where significant turbulence-chemistry interaction occurs, the magnitudes of the background scalar fluctuations are much smaller, thereby having negligible effects on the estimated resolution. Consequently, the revised model was not used here.
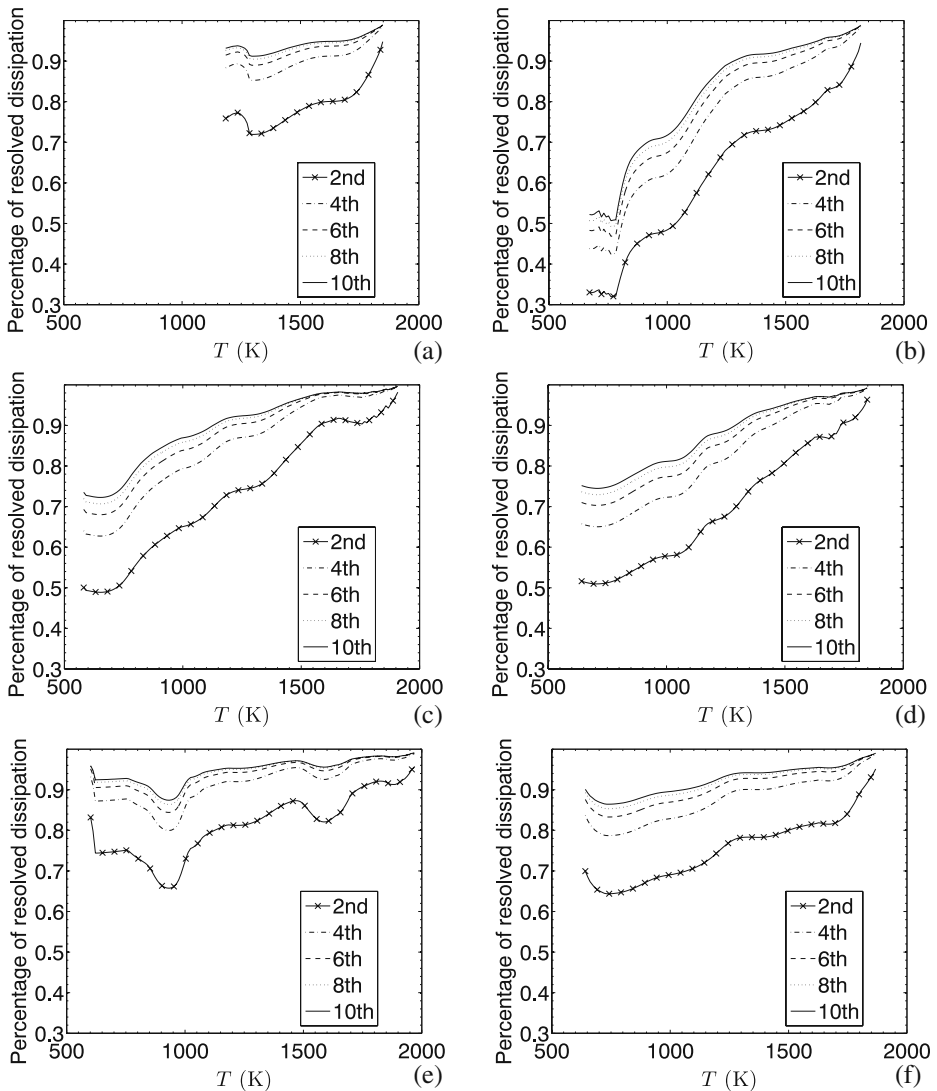
Fig. 15 Estimation of the resolved dissipation rate as a function of temperature. **a**, **c**, **e** Flame D at $x/d = 7.5$, 15, and 30, respectively; **b**, **d**, **f** flame E at the same locations

5 Conclusions

The recently developed conditional sampling-based method for noise correction and resolution estimation for scalar dissipation rate measurements [12] was used to study turbulent partially premixed flames (Sandia flames D and E). The well-resolved conditional local scalar fields were analyzed to obtain the variance of the measurement noise at each measurement location. The noise variance was used to correct the dissipation rate of these fields as well as the mean and conditional dissipation rate.

The results show that the noise variance determined is accurate and the noise correction procedure is capable of removing the noise contributions from the measured dissipation rate. The mean dissipation rate is well resolved at all measurement locations except perhaps at $x/d = 7.5$ in flame E, where the resolution is sightly worse. The conditional dissipation rate is also well resolved at all locations in both flames D and E.

The potentially under-resolved fields were analyzed with the error-function model to estimate the length scale and the extent of resolution of these fields after their dissipation rate is corrected for noise. The effects of the finite sampling volume (pixel size) on the resolution were included in the model calculation in addition to that of the finite sampling interval. The ratios of the measured dissipation rate using finite difference schemes of second- to tenth-orders were compared to model calculations to infer the width of the scalar (ramp-cliff) structure. The results show that the dissipation rate filtered conditionally on the mixture fraction is quite well resolved for these local fields. Because these fields have dissipation rate values much larger than the mean dissipation rate, the latter is better resolved.

We further analyzed the dissipation rate filtered conditionally on the both the mixture fraction and temperature, again focusing on the local fields with large SFS variance values. The dissipation length scale increases with downstream distance, and is larger in flame D. At each location, the length scale decreases with temperature, in some cases by a factor of three from 1,800 K to 750 K. The ramp-cliff structure is generally quite well resolved ($>90\%$) for temperatures higher than 1,300 K. At lower temperatures the length scale of the ramp-cliff structure is smaller, with the value at 700 K being approximately one half of those at 1,800 K. As a result, the percentage of the dissipation rate resolved is lower. The results show that to fully resolve these fields with low temperatures, which are extinguished flamelets, the pixel size needs to be reduced by approximately one half. We note that these are events with low probability, consequently the majority of the scalar fields are well resolved.

The present study demonstrated the effectiveness of the conditional-sampling method. The error function as a model for the ramp-cliff structure was also found to provide highly self-consistent results. The observed variations of the dissipative length scale with the Reynolds number, the measurement location, and the temperature provide a basis for further understanding of the physics of the small-scale scalar in turbulent flames.

References

1. Bilger, R.W.: The structure of turbulent nonpremixed flames. In: Proceedings of the Twenty-Second Symposium (International) on Combustion, pp. 475–488 (1988)
2. Peters, N.: Turbulent Combustion. Cambridge University Press, Cambridge (2000)
3. Pope, S.B.: PDF methods for turbulent reacting flows. Prog. Eng. Combust. Sci. **11**, 119–192 (1985)
4. Bilger, R.: Conditional moment closure for turbulent reacting flow. Phys. Fluids A **5**, 436–444 (1993)

5. Peters, N.: Laminar diffusion flamelet models in non-premixed turbulent combustion. Prog. Eng. Combust. Sci. **10**, 319–339 (1984)
6. Eswaran, V., Pope, S.B.: Direct numerical simulations of the turbulent mixing of a passive scalar. Phys. Fluids **31**, 506–520 (1988)
7. Wyngaard, J.C.: Measurements of small-scale turbulence structure with hot wires. J. Sci. Instrum. **1**, 1105–1108 (1968)
8. Brown, L.W.B., Antonia, R.A., Chambers, A.J.: Effects of the separation between cold wires on the spatial derivatives of temperature in a turbulent flow. Boundary - Layer Meteorol. **27**, 129–139 (1983)
9. Dahm, W.J.A., Southerland, K.B.: Quantitative flow visualization via fully resolved four-dimensional spatio-temporal imaging. In: Smits, A., Lim, T.T. (eds.) Flow Visualization: Techniques and Examples, pp. 289–316. Imperial College Press, London (2000)
10. Mi, J., Nathan, G.J.: The influence of probe resolution on the measurement of a passive scalar and its derivatives. Exp. Fluids **34**, 687–696 (2003)
11. Sutton, J., Driscoll, J.: A method to simultaneously image two-dimensional mixture fraction, scalar dissipation rate, temperature and fuel consumption rate fields in a turbulent non-premixed jet flame. Exp. Fluids **41**, 603–627 (2006)
12. Cai, J., Tong, C.: A conditional sampling-based method for noise and resolution corrections for scalar dissipation rate measurements. Phys. Fluids **21**, 065104 (2009)
13. Wang, G.-H., Clemens, N.T., Barlow, R.S., Varghese, P.L.: A system model for assessing scalar dissipation measurement accuracy in turbulent flows. Meas. Sci. Technol. **18**, 1287–1303 (2007)
14. Wang, G., Karpetis, A.N., Barlow, R.S.: Dissipation length scales in turbulent nonpremixed jet flames. Combust. Flame **148**, 62–75 (2007)
15. Pope, S.B.: Turbulent Flows. Cambridge University Press, Cambridge (2000)
16. Wang, G.-H., Clemens, N.T., Varghese, P.L.: Two-point, high-repetition-rate Rayleigh thermometry in flames: techniques to correct for apparent dissipation induced by noise. Appl. Opt. **44**, 6741–6751 (2005)
17. Kaiser, S.A., Frank, J.H.: Imaging of dissipative structures in the near field of a turbulent non-premixed jet flame. Proc. Combust. Inst. **31**, 1515–1523 (2007)
18. Frank, J.H., Kaiser, S.A.: High-resolution imaging of dissipative structures in a turbulent non-premixed jet flame with laser Rayleigh scattering. Exp. Fluids **44**, 221–233 (2008)
19. Tong, C., Warhaft, Z.: On passive scalar derivative statistics in grid turbulence. Phys. Fluids **6**, 2165–2176 (1994)
20. Wang, D., Tong, C.: Conditionally filtered scalar dissipation, scalar diffusion, and velocity in a turbulent jet. Phys. Fluids **14**, 2170–2185 (2002)
21. Wang, D., Tong, C., Barlow, R.S., Karpetis, A.N.: Experimental study of scalar filtered mass density function in turbulent partially premixed flames. Proc. Combust. Inst. **31**, 1533–1541 (2007)
22. Cai, J., Wang, D., Tong, C., Barlow, R.S., Karpetis, A.N.: Investigation of subgrid-scale mixing of mixture fraction and temperature in turbulent partially premixed flames. Proc. Combust. Inst. **32**, 1517–1525 (2009)
23. Karpetis, A.N., Barlow, R.S.: Measurements of scalar dissipation in turbulent piloted methane/air jet flames. Proc. Combust. Inst. **29**, 1929–1936 (2002)
24. Barlow, R.S., Karpetis, A.N.: Measurements of scalar variance, scalar dissipation, and length scales in turbulent piloted methane/air jet flames. Flow Turbul. Combust. **72**, 427–448 (2004)
25. Karpetis, A.N., Barlow, R.S.: Measurements of flame orientation and scalar dissipation in turbulent partially premixed methane flames. Proc. Combust. Inst. **30**, 665–672 (2005)
26. Tong, C.: Measurements of conserved scalar filtered density function in a turbulent jet. Phys. Fluids **13**, 2923–2937 (2001)
27. Zhang, H., Wang, D., Tong, C.: On conditional scalar increment and joint velocity-scalar increment statistics. New J. Phys. **6**, 38 (2004)
28. Bilger, R., Starner, S., Kee, R.: On reduced mechanisms for methane-air combustion in non-premixed flames. Combust. Flame **80**, 135–149 (1990)
29. Barlow, R.S., Karpetis, A.N.: Scalar length scales and spatial averaging effects in turbulent piloted methane/air jet flames. Proc. Combust. Inst. **30**, 673–680 (2005)
30. Barlow, R.S., Frank, J.H., Karpetis, A.N., Chen, J.Y.: Piloted methane/air jet flames: Transport effects and aspects of scalar structure. Combust. Flame **143**, 433–449 (2005)